Rare Met. (2021) 40(11):3205–3214
https://doi.org/10.1007/s12598-020-01681-1

RARE METALS

ORIGINAL ARTICLE

Ionic liquid-induced ultrathin and uniform N-doped carbon-wrapped T-Nb_2O_5 microsphere anode for high-performance lithium-ion battery

Rui-Xue Sun, Yang Yue, Xin-Feng Cheng, Ke Zhang, Su-Ying Jin, Guang-Yin Liu*, Yu-Xin Fan, Yan Bao, Xiao-Di Liu*

Received: 26 March 2020 / Revised: 9 June 2020 / Accepted: 10 December 2020 / Published online: 2 March 2021

Abstract Orthorhombic-phase Nb_2O_5 (T-Nb_2O_5) has been widely investigated as an intercalation anode material for Li-ion batteries due to the larger interplanar lattice spacing and high safety. However, its applications are limited by the intrinsic low electric conductivity. Herein, an ultrathin N-doped carbon-coating layer was constructed on porous T-Nb_2O_5 microspheres uniformly via a convenient thermal treatment method with ionic liquid as a carbon precursor. The synthesized T-Nb_2O_5@N–C exhibits significantly enhanced rate capability (155.5 mAh·g^{-1} at 20C) than initial T-Nb_2O_5 (110.2 mAh·g^{-1} at 20C). Besides, T-Nb_2O_5@N–C shows ultralong cycle life, with only a 0.02% decrease in the capacity per cycle at a high current density of 10C. The corresponding electrochemical tests show that the preferable rate capability of T-Nb_2O_5@N–C electrode is attributed to the increased electronic conductivity and pseudocapacitance contribution induced by ultrathin surface N-doped carbon layer. On the other hand, the mesoporous structure of T-Nb_2O_5@N–C ensures fast Li$^+$ diffusion dynamics and electrolyte penetration. Furthermore, T-Nb_2O_5@N–C also performs well in a $LiNi_{0.5}Mn_{0.3}Co_{0.2}O_4$‖T-$Nb_2O_5$@N–C full cell. This work provides a facile method to construct integrated anode materials for potential applications in lithium-ion batteries.

Keywords Ionic liquid; Ultrathin N-doped carbon; T-Nb_2O_5; Lithium-ion battery; Full cell

1 Introduction

Renewable energy sources, such as solar, wind and geothermal, have been developed in large scale to mitigate the increasingly serious oil shortage and air pollution [1–3]. The large-scale energy-storage technology is one of the critical factors for the development of renewable energy resources. Among them, lithium-ion battery (LIB) as an energy-storage device has drawn discernible attention that can meet the applications with its low self-discharge, high energy density and long cycle life [4–6]. Graphite is the most widely used commercial anode material for LIB due to its low cost, good specific capacity and cyclic stability [7–9]. Nevertheless, due to the working voltage of graphite under 1.0 V (vs. Li$^+$/Li), the nonconductive solid–electrolyte interphase film would be generated on the material surface. Furthermore, the graphite material also along with huge volume changes ($\sim$ 9%) from C to Li_xC_6 ($0 < x < 6$) process. The issues would cause a capacity loss and potential safety issue in actual use.

To solve the above problems, plenty of anode materials of LIBs have been investigated. In particular, the transition

---

Rui-Xue Sun and Yang Yue have contributed equally to this work.

Electronic supplementary material The online version of this article (https://doi.org/10.1007/s12598-020-01681-1) contains supplementary material, which is available to authorized users.

R.-X. Sun, X.-F. Cheng, K. Zhang, S.-Y. Jin,
G.-Y. Liu*, Y.-X. Fan, Y. Bao, X.-D. Liu*
College of Chemistry and Pharmaceutical Engineering,
Engineering Technology Research Center of Henan Province for
Solar Catalysis, Nanyang Normal University, Nanyang 473061,
China
e-mail: liugy13@163.com

X.-D. Liu
e-mail: liuxiaodiny@126.com

Y. Yue
College of Science, Henan Agricultural University, Zhengzhou
450001, China

metal oxides can acquire and deliver high reversible capacities and work in high potential for a high-energy LIBs, which have been investigated as electrode materials [10–15]. Among them, orthorhombic niobium oxide is thought to be a promising anode material for LIBs based on the considerable theoretical capacity with multiple redox couples, minimal volume change (3%) upon cycling and excellent rate capability [11, 16, 17]. Also, the appropriate voltage of niobium oxide (1.0–2.0 V vs. Li^+/Li) can effectively prevent the formation of Li dendrites and improve the safety of LIBs. However, the moderate Li^+ diffusion dynamics and poor electrical conductivity (3.4×10^{-6} $S \cdot cm^{-1}$ at 300 K) of bulk Nb_2O_5 material greatly limit its high rate capability, which is a critical factor for the application of LIBs. Therefore, great efforts have been explored to promote the ion diffusion rate and elevate the electrical conductivity of Nb_2O_5 electrodes. Well-designed nanostructures of electrodes can effectively shorten the distance of Li^+ diffusion. For instance, Lou et al. [18] found that three-dimensionally ordered macroporous orthorhombic Nb_2O_5 prepared by hard template method exhibited a remarkably high rate performance. Fu et al. [19] fabricated yolk–shell-structured Nb_2O_5 microspheres via spray-drying method to enhance the electronic conductivity and rate capability of the electrode. However, the high cost, complex synthetic process and harsh preparative conditions of Nb_2O_5 are restricting the practical perspective.

Apart from Li^+ diffusion, the poor electric conductivity of Nb_2O_5 electrode is the other important constraint for rate performance. Coating conductive materials on the electrode is an efficient way to facilitate charge migration. It is worth noting that the heteroatom (N, B, S, and P)-doped carbon material with high electrical conductivity is an ideal candidate for coated layer [20–22]. Nitrogen element has been widely introduced into the carbon material; it can not only create vast defects and active sites to motivate the redox operation, but also enhance the electronic conductivity with the faster reaction kinetics. Furthermore, an ionic liquid was extensively used as raw materials for nitrogen and carbon to obtain N-doped graphitized carbon. Owing to the fluidic properties of ionic liquid, it can more easily penetrate porous materials than the conventional carbon sources and then can form the thin uniform coating layer on the materials surface, which would not change the porous surface characteristics [23, 24]. Therefore, ionic liquid-induced N-doped graphitized carbon coating has shown a prominent prospect for solving the poor electric conductivity of Nb_2O_5 electrode.

Herein, we report the ultrathin N-doped carbon-coated porous T-Nb_2O_5 microsphere prepared through a simple and convenient thermal treatment strategy. N and C are introduced to the electrode material through the impregnation of ionic liquid. N-doped carbon networks can offer high electrical conductivity. On the other hand, the porous structure can shorten the transfer path of electrons and ions to further promote the rate performance. Therefore, the as-synthesized T-Nb_2O_5@N–C demonstrates a high specific capacity (221.7 $mAh \cdot g^{-1}$ at 1C) and superior rate capability (155.5 $mAh \cdot g^{-1}$ at 20C). The incorporation of an ionic liquid as the coating layer material and structural modification of T-Nb_2O_5 to improve the excellent long cycling life is an imperative strategy, which is suitable for being widely used in electrode material design (Scheme 1).

2 Experimental

2.1 Preparation of T-Nb_2O_5

About 2.7 g $NbCl_5$ was completely dissolved to 80 ml ethylene glycol with vigorous stirring. The solution was then retained at 200 °C for 24 h by the solvothermal method. Subsequently, the precursor precipitate was collected and washed with water and ethanol several times. After that, the precursor was put in a muffle furnace and heated at 600 °C for 2 h to obtain the final products T-Nb_2O_5.

2.2 Preparation of T-Nb_2O_5@N–C

At room temperature, 100 μl ionic liquid (1-ethyl-3-methylimidazolium dicyanamide), 0.4 g T-Nb_2O_5 and 10 ml acetone were mixed with vigorous stirring until the evaporation of the solvent. After that, the mixture was calcined under N_2 at 600 °C for 2 h to obtain the T-Nb_2O_5@N–C.

2.3 Characterizations

X-ray diffractometer (XRD, Dmax/2500PC) was used to determine the crystalline phase of the materials with a scanning rate of 2 $(°) \cdot min^{-1}$. The morphologies and microstructures were surveyed using a scanning electron microscope (SEM, ZEISS SIGMA 500) and a field

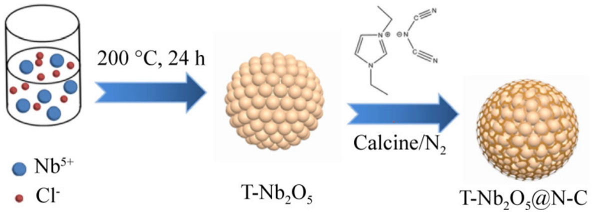

Scheme 1 Synthesis processes of N-doped carbon wrapped T-Nb_2O_5 microsphere

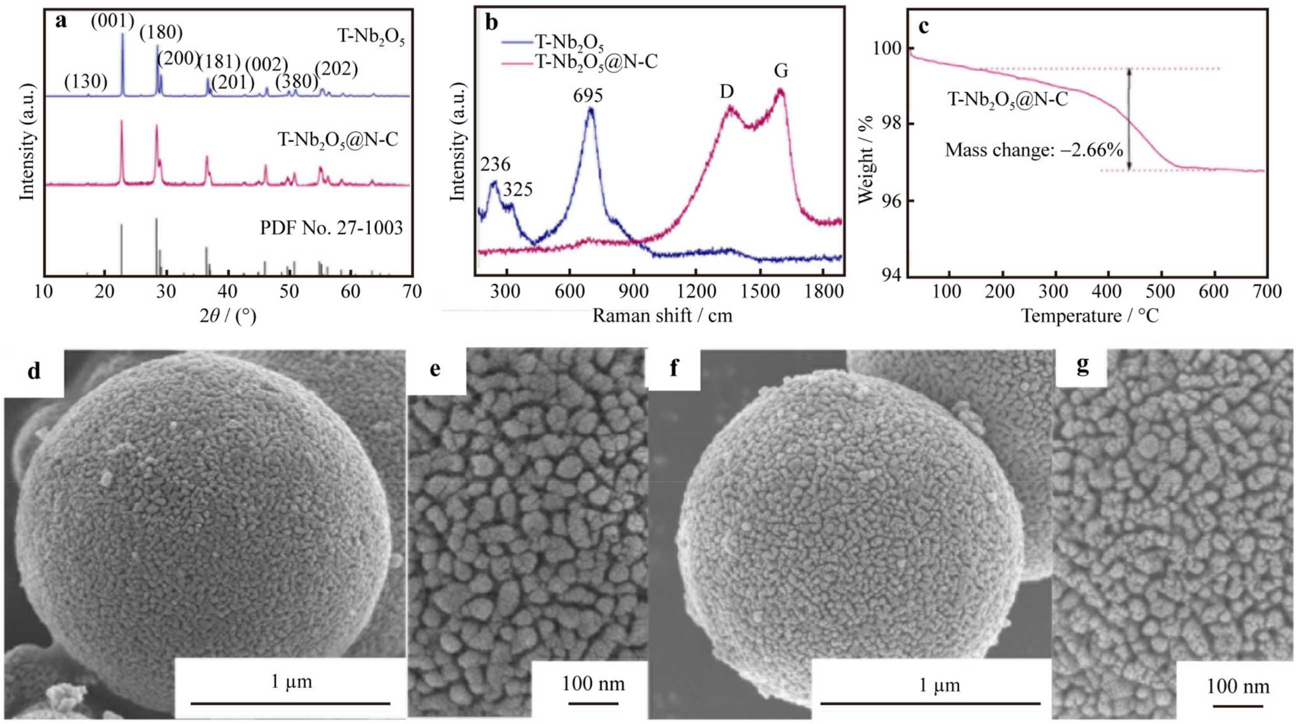

Fig. 1 **a** XRD patterns and **b** Raman spectra of T-Nb_2O_5 and T-Nb_2O_5@N–C; **c** TG analysis of T-Nb_2O_5@N–C; SEM images of **d, e** T-Nb_2O_5 and **f, g** T-Nb_2O_5@N–C

emission transmission electronic microscope (FETEM, JEM-2100). Energy-dispersive X-ray spectroscopy (EDS) was employed to analyze elemental composition and distribution on the surface. The Brunauer–Emmett–Teller (BET) surface area and pore volume were identified by N_2 adsorption–desorption isotherm (Micromeritics ASAP 2020 analyzer). The carbon contents in the composites were measured by thermal gravimetric analysis (TG, SDT Q600). The valence states of the key elements in samples were studied by X-ray photoelectron spectroscopy (XPS, Thermo ESCALAB 250XI electron spectrometer, Al Kα radiation). Raman spectroscopy (LabRAM HR Evolution, excited by 532-nm laser) was employed to investigate the structural characteristic of carbonaceous materials in the products. The electrical conductivity of the T-Nb_2O_5@N–C and T-Nb_2O_5 was directly measured by semiconductor powder resistivity tester (ST2722) and ultra-high-resistance microcurrent tester (ST2643).

2.4 Electrochemical measurements

The electrode sheets were composed of T-Nb_2O_5 or T-Nb_2O_5@N–C powder, acetylene black and polyvinylidene fluoride (mass ratio of 70:20:10) in the N-methyl-2-pyrrolidone. The mixtures were uniformly cast on Cu foil and were put in a vacuum oven at 120 °C overnight. The loading amount of the electrode was around 2 $mg \cdot cm^{-2}$. The full battery was constructed of commercial $LiNi_{0.5}Mn_{0.3}Co_{0.2}O_4$ and T-Nb_2O_5@N–C material as cathode and anode with a mass ratio of 1.4:1. The preparation process of $LiNi_{0.5}Mn_{0.3}Co_{0.2}O_4$ electrode is consistent with that of T-Nb_2O_5@N–C. All samples were evaluated using CR2025 coin cells with lithium metal as the counter and 1 $mol \cdot L^{-1}$ $LiPF_6$ dissolved in ethylene carbonate (EC)/diethyl carbonate (DEC) /dimethyl carbonate(DC) (1:1:1 in volume ratio) as the electrolyte. The LANDCT2001A system was used to test the electrochemical performance with the potential range of 1.0–3.0 V at ambient temperature. The electrochemical capacities of the samples were tested with the quality of active material. Cycling voltammetry (CV) and electrochemical impedance spectroscopy (EIS) measurements were performed using a CHI 650D electrochemical workstation.

3 Results and discussion

In Fig. 1a, the crystalline phase of T-Nb_2O_5 and T-Nb_2O_5@N–C was analyzed by XRD. All the strong diffraction peaks in both samples can be indexed to orthorhombic Nb_2O_5 with a *Pbam* space group (PDF No. 27-1003) [25]. Besides, no carbon peaks can be observed due to that carbon is amorphous or the content of carbon is

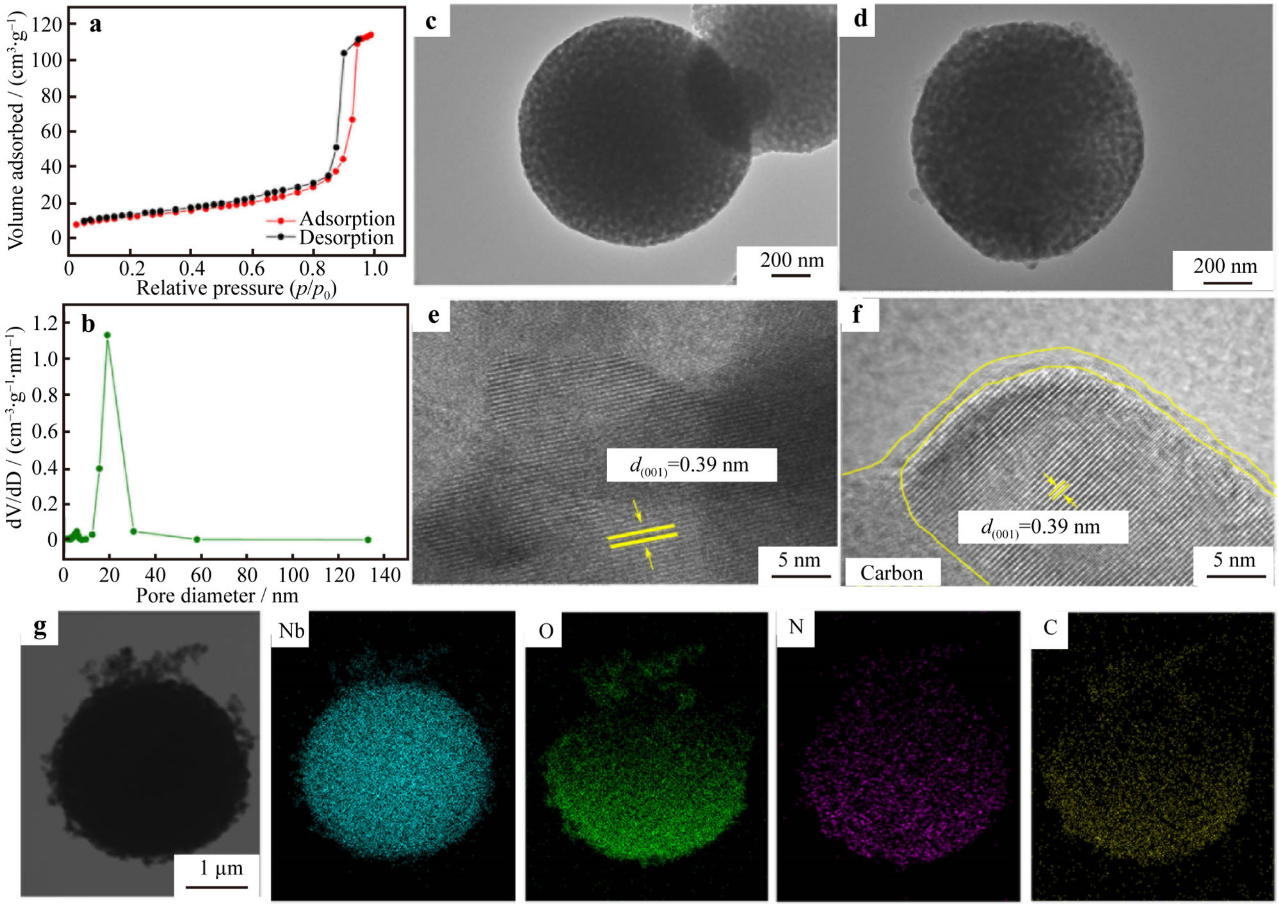

Fig. 2 **a** Nitrogen adsorption–desorption isotherms and **b** pore size distribution of T-Nb_2O_5@N–C; TEM and HRTEM images of **c**, **e** T-Nb_2O_5 and **d, f** T-Nb_2O_5@N–C; **g** elemental mappings of T-Nb_2O_5@N–C

low. This result suggests that high-purity Nb_2O_5 composites for the two samples have been synthesized. To verify the presence of Nb_2O_5 and carbon in samples, Raman spectra are shown in Fig. 1b. The peaks in the range of 200–500 cm^{-1} and 695 cm^{-1} for the T-Nb_2O_5 in Fig. 1b are assigned to bending vibration and stretching vibration of the Nb–O–Nb bond, respectively [26, 27]. Meanwhile, T-Nb_2O_5@N–C along with the introduction of ionic liquids has two strong peaks at around 1362 and 1609 cm^{-1}, deriving from D-band and G-band of carbon, respectively [28]. However, the characteristic peaks of the Nb–O–Nb bond have disappeared for T-Nb_2O_5@N–C, suggesting that the tight carbon-coating layer may screen the signal [29]. The ratio of the D-band to G-band intensities (I_D/I_G) is 0.92, certifying the graphitic N-doped carbon in T-Nb_2O_5@N–C sample [30]. The carbon content in T-Nb_2O_5@N–C is verified as 2.66% by TG analysis (Fig. 1c).

It is reported that the microstructure of the materials is closely related to the electrochemical performance. We thus investigated the morphology of T-Nb_2O_5 and T-Nb_2O_5@N–C. As displayed in Fig. 1d, e, T-Nb_2O_5 microsphere with the size of ~ 2.5 μm is composed of uniform primary nanoparticles (~ 50 nm). After the introduction of N-doped carbon, the size and shape of T-Nb_2O_5@N–C do not change obviously and the porous microsphere structure is maintained, as shown in Fig. 1f. The nitrogen adsorption–desorption isotherm (Fig. 2a) indicates BET surface area of T-Nb_2O_5@N–C of 59 $m^2 \cdot g^{-1}$, and T-Nb_2O_5@N–C has rich mesopores with a size of ~ 20 nm (Fig. 2b), in accord with SEM results (Fig. 1g). These results demonstrate that the porous T-Nb_2O_5@N–C microsphere has been synthesized. This mesoporous structure would expedite electrolyte penetration and then promote Li^+ diffusion dynamics.

The detailed morphology of T-Nb_2O_5 and T-Nb_2O_5@N–C was then investigated by TEM and HRTEM, as displayed in Fig. 2c–f. T-Nb_2O_5@N–C exhibits similar microsphere morphology with T-Nb_2O_5. Besides, HRTEM images in Fig. 2e, f show the interplanar distance of 0.39 nm in both of the two samples, which can be well indexed to the (001) plane of orthorhombic Nb_2O_5, corresponding to XRD results in Fig. 1a. The empty octahedral sites between its (001) planes can result in high

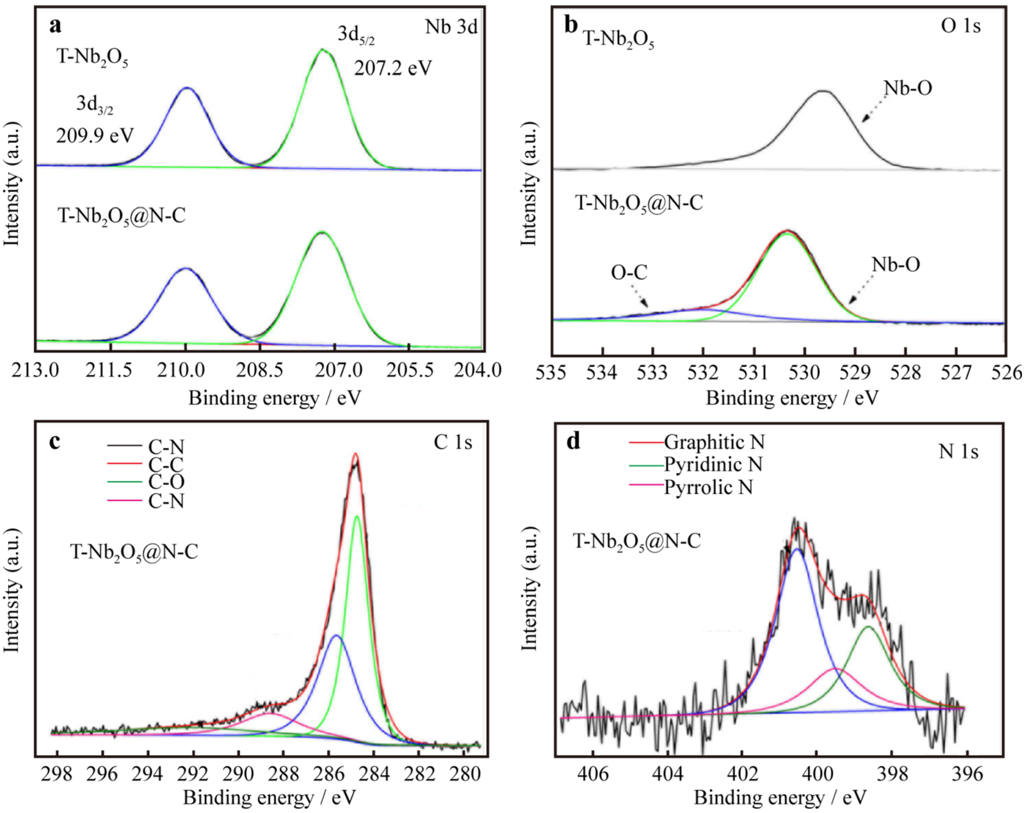

Fig. 3 **a** Nb 3d and **b** O 1 s high-resolution XPS spectra of T-Nb_2O_5 and T-Nb_2O_5@N–C; **c** C 1 s and **d** N 1 s XPS spectra of T-Nb_2O_5@N–C

rate capability [31]. In HRTEM image of T-Nb_2O_5@N–C (Fig. 2f), the ultrathin uniform N-doped carbon layer (~ 2 nm) is coated on Nb_2O_5 nanoparticles, as marked by the bright yellow line. The intimate contact of the carbon layer and Nb_2O_5 will facilitate charge transfer to deliver high capacity during the charge/discharge process [32]. The elemental mapping was implemented to investigate the material surface, and the elemental distribution of Nb, O, N and C is shown in Fig. 2g. EDS result of the T-Nb_2O_5@N–C powder is recorded in Fig. S1. N content in T-Nb_2O_5@N–C is 0.21%. The above results confirm the porosity and uniform distribution of N-doped carbon. As suggested from previous literature, the ultrathin and uniform coating of N-doped carbon is an ideal way for accelerating electrons transport.

XPS measurements were carried out to elucidate the surface chemical states and confirm the bonding relationship. Figure 3a, b shows the high-resolution Nb and O spectra of T-Nb_2O_5 and T-Nb_2O_5@N–C, respectively. In Fig. 3a, two predominant peaks at 207.2 and 209.9 eV are assigned to Nb $3d_{5/2}$ and Nb $3d_{3/2}$, which are Nb^{5+} state in both samples [33]. Compared to the O 1s spectra for T-Nb_2O_5, the peaks of T-Nb_2O_5@N–C shift to the high binding energy. Additionally, the newly formed C–O (531.6 eV) for T-Nb_2O_5@N–C is demonstrated in Fig. 3b, indicating the formation of C–O–Nb bonds during the thermal treatment process [34]. The C 1s spectra consist of four peaks including binding energies of 284.5, 285, 287 and 290 eV, which respectively represent the carbon functional group with C–C, C–N, C=N and C–O in Fig. 3c [35]. As displayed in Fig. 3d, N 1s spectrum can be divorced into three peaks with binding energies of 398.6, 400.8 and 403.5 eV, corresponding to pyridinic N, pyrrolic N and graphitic N, respectively [36]. The results further indicate that the N-doped carbon has been successfully coated on Nb_2O_5 material with ionic liquid as nitrogen and carbon source. N for electrode material was adopted to provide supererogatory reactive sites and degrade the energy barrier for Li^+, which can dramatically improve the Li-ion storage properties.

Figure 4a, b depicts representative galvanostatic charge/discharge profiles of T-Nb_2O_5 and T-Nb_2O_5@N–C at different current densities. The potential difference between charge and discharge curves of T-Nb_2O_5@N–C is less than that of T-Nb_2O_5, suggesting the low polarization of T-Nb_2O_5@N–C, which is propitious for practical demand. Compared with T-Nb_2O_5, the carbon-coating sample shows better rate performances, as shown in Fig. 4c. The discharge capacitances of T-Nb_2O_5 decrease (185.1, 160.6, 150.8, 132.3 and 110.2 $mAh \cdot g^{-1}$) with current density increasing from 1C to 20C. At the rates of 1C, 2C, 5C, 10C and 20C, T-Nb_2O_5@N–C shows reversible capacities of

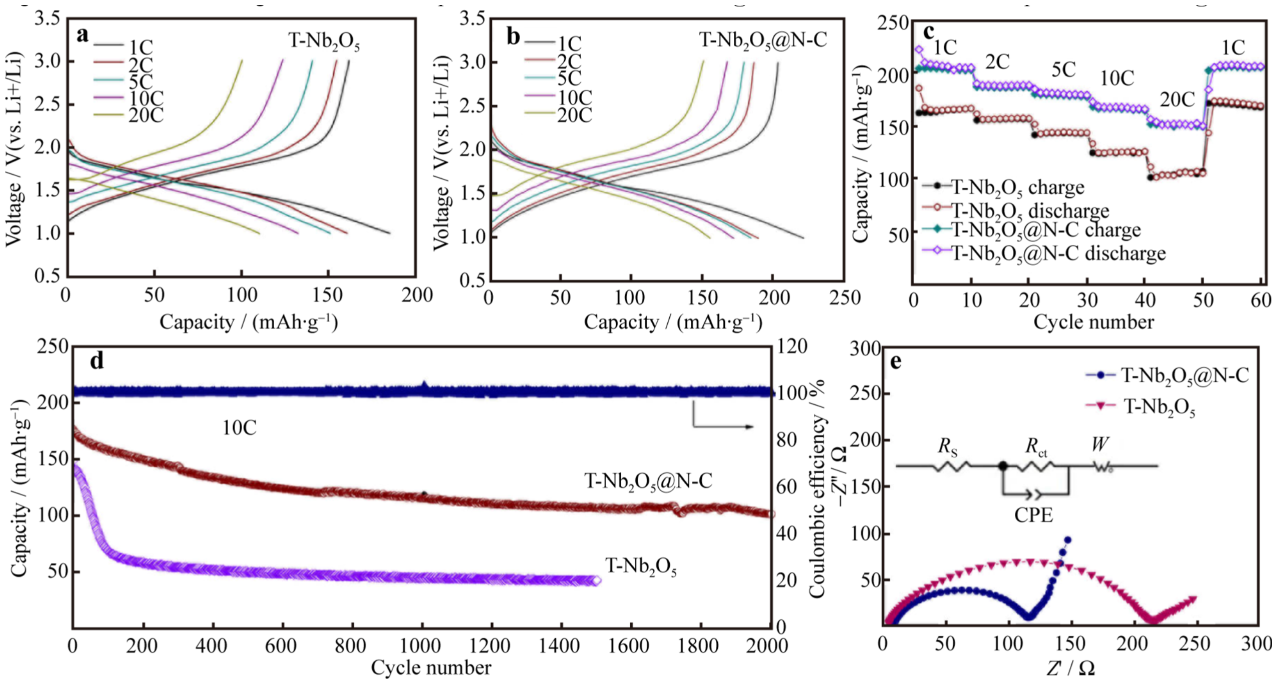

Fig. 4 Galvanostatic discharge/charge curves of **a** T-Nb$_2$O$_5$ and **b** T-Nb$_2$O$_5$@N–C at 1C, 2C, 5C, 10C, 20C current densities; **c** rate performance and **d** cycle performance of T-Nb$_2$O$_5$ and T-Nb$_2$O$_5$@N–C; **e** EIS spectra of T-Nb$_2$O$_5$ and T-Nb$_2$O$_5$@N–C and corresponding equivalent circuit

Table 1 Comparison of electrochemical performance for the same reported Nb$_2$O$_5$-based materials

Active materials	Rate capability/(mAh·g^{-1})	Cyclability/(mAh·g^{-1})	Refs.
T-Nb$_2$O$_5$@N–C	172.1 (10C); 155.5 (20C)	101.1 (2000 cycles, 10C)	This work
Three-dimensional macroporous T-Nb$_2$O$_5$	106.0 (20C)	124.0 (100 cycles, 10C)	[18]
Yolk–shell Nb$_2$O$_5$	138.0 (10C)	–	[19]
T-Nb$_2$O$_5$ nanoparticles	–	111.7 (100 cycles, 10C)	[30]
T-Nb$_2$O$_5$/rGO	210.0 (10C)	163.0 (1000 cycles, 10C)	[37]
Wired H-Nb$_2$O$_5$	100.0 (10C) 80.0 (20C)	120.0 (150 cycles, 0.5C)	[38]

221.7, 189.6, 184.3, 172.1, and 155.5 mAh·g^{-1}, respectively. When current density returns to 1C, the electrode recovers 204.6 mAh·g^{-1}, revealing the excellent reversible capability of T-Nb$_2$O$_5$@N–C. The cycling performance at high current density is an important parameter to further illustrate lifespan of the electrode in practical application. Impressively, T-Nb$_2$O$_5$@N–C shows excellent longevity life and superior capacity retention (Fig. 4d). The initial cycle of T-Nb$_2$O$_5$@N–C capacitance is 176.4 mAh·g^{-1} at 10C, and it keeps a capacity of 101.1 mAh·g^{-1} at the 2000 cycles with a higher capacity retention of 57.3%. However, after the first cycle (147.6 mAh·g^{-1}), the specific capacity of T-Nb$_2$O$_5$ continues to decrease until the 100th cycle is stable. The capacity of T-Nb$_2$O$_5$ only remains 42.6 mAh·g^{-1} after 1500 cycles with a capacity retention of 28.8%. In addition, the Coulombic efficiency of T-Nb$_2$O$_5$@N–C is found to be nearly 100% in each cycle. Table 1 shows the comparison of electrochemical performances of some Nb$_2$O$_5$-based anode materials, which are taken from the previous typical reports with excellent performances in LIBs [18, 19, 30, 37, 38]. This result demonstrates that the active site of N atom and conductive carbon material can not only improve the effective electron transmission path for the high rate capability, but also inhibit structure pulverization after long-periodic cycling.

EIS and CV measurements of T-Nb$_2$O$_5$@N–C were further investigated to analyze electrode kinetics for Li-storage. According to the equivalent circuit fitting (Fig. 4e), the calculated charge transfer resistance (R_{ct} = 102 Ω) is smaller than that of T-Nb$_2$O$_5$ (R_{ct} = 204 Ω). It is

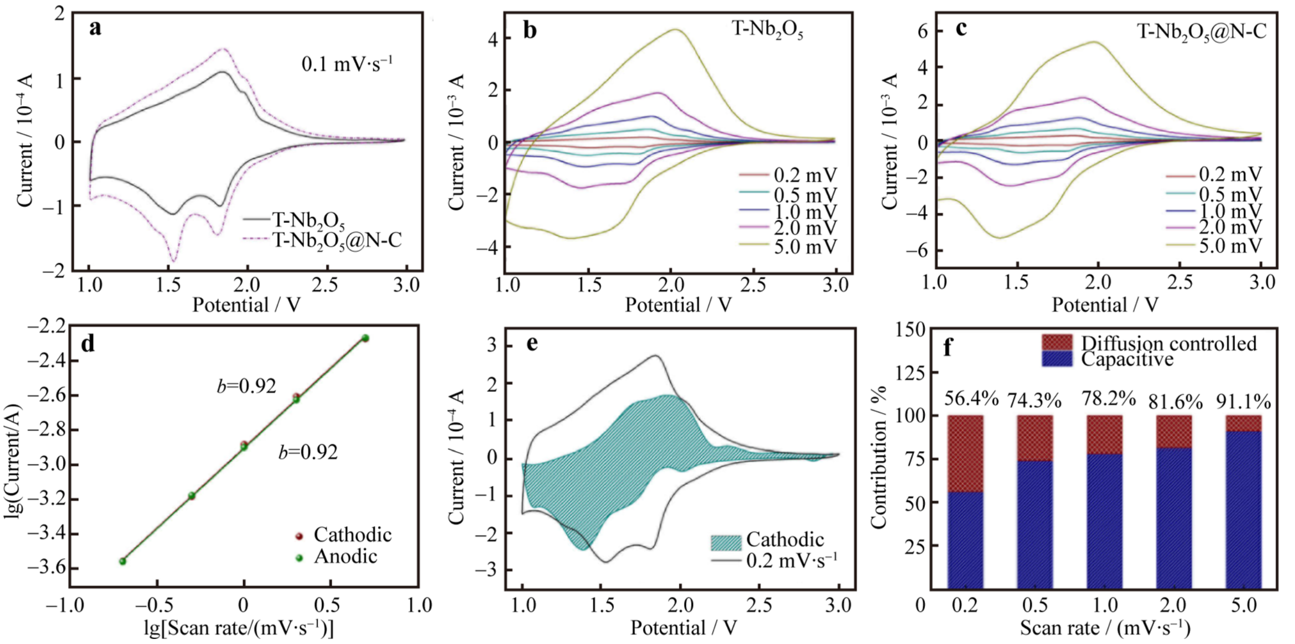

Fig. 5 **a** CV curves of T-Nb_2O_5 and T-Nb_2O_5@N–C at 0.1 mV·s^{-1}; CV curves of **b** T-Nb_2O_5 and **c** T-Nb_2O_5@N–C at different scan rates from 0.2 to 5.0 mV·s^{-1}; **d** *b* values determined by the relationship between peak current and sweep rate of T-Nb_2O_5@N–C; **e** capacitive contribution (green shaded regions) in CV test of T-Nb_2O_5@N–C at 0.2 mV·s^{-1}; **f** contributions of capacitive and diffusion-controlled capacities at different sweep rates of T-Nb_2O_5@N–C

suggesting that the enhanced electric conductivity of T-Nb_2O_5@N–C is attributed to the surface modification of N-doped carbon. The effect of N-doped carbon network on the electrical properties of T-Nb_2O_5@N–C can be researched by the four-point probe setup. The electrical conductivity of the T-Nb_2O_5@N–C can be one or two orders of magnitude better than that of T-Nb_2O_5 at the same intensity of pressure (Fig. S2), due to the addition of N-doped carbon network. Therefore, the increased electrical conductivity in this work clearly supports the formation of additional conductive paths between N-doped carbon network and T-Nb_2O_5. CV curves of T-Nb_2O_5 and T-Nb_2O_5@N–C with a voltage range of 1.0–3.0 V are shown in Fig. 5. Clearly, two oxidation peaks at 1.85 and 1.98 V and two strong reduction peaks at 1.85 and 1.53 V of the two samples both can be observed in Fig. 5a at 0.1 mV·s^{-1} [39]. The main electrochemical reaction is between Nb^{5+} and Nb^{3+} in the process of intercalation/deintercalation of Li^+. The two reduction peaks are corresponding to the valence state from Nb^{5+} to Nb^{3+}, indicating the Li^+ intercalation into the Nb_2O_5. On the contrary, the oxidation peaks reflect lithium-ion extraction process of $Li_xNb_2O_5$. The specific process is shown in Eq. (1):

$$Nb_2O_5 + xLi^+ + xe^- \Leftrightarrow Li_xNb_2O_5, \tag{1}$$

where $x \leq 2$ (corresponding to 200 mAh·g^{-1}). The main reduction and oxidation peaks location could be explained to the out and in of Li^+ from orthorhombic Nb_2O_5 crystal structure.

To further explore the kinetics of T-Nb_2O_5@N–C electrode, the CV curves at different scan rates were carried out on T-Nb_2O_5 and T-Nb_2O_5@N–C (Fig. 5b, c). At the same sweep speed, CV curves of the two samples have similar peak patterns, suggesting the same obvious redox reactions along with Li^+ insertion/extraction. It is worth noting that T-Nb_2O_5@N–C electrode exhibits much smaller polarization than T-Nb_2O_5 at 5.0 mV·s^{-1}, demonstrating better electrochemical reversibility for T-Nb_2O_5@N–C at high current density. As reported by previous studies for CVs [37, 40], the total charge storage of electrodes could be separated into two parts: the contribution of Li^+ insertion/extraction controlled by diffusion and the surface-controlled capacitive contribution. The linear relationship between the peak currents (i) and the scan rates (v) in log operation follows the equations:

$$i = av^b \tag{2}$$

$$\lg i = \lg a + b \lg v \tag{3}$$

where b value can provide the charge storage mechanism during the electrochemical process. The b value approaching to 0.5 means that the process is completely limited by diffusion. Contrarily, the capacity is controlled by surface-controlled capacitive behavior when the b value accesses to 1. As shown in Fig. 5d, the slope b values of cathode and anode are both 0.92, illustrating that the electrochemical reactions of T-Nb_2O_5@N–C are mainly dominated by the surface-controlled capacitive behavior

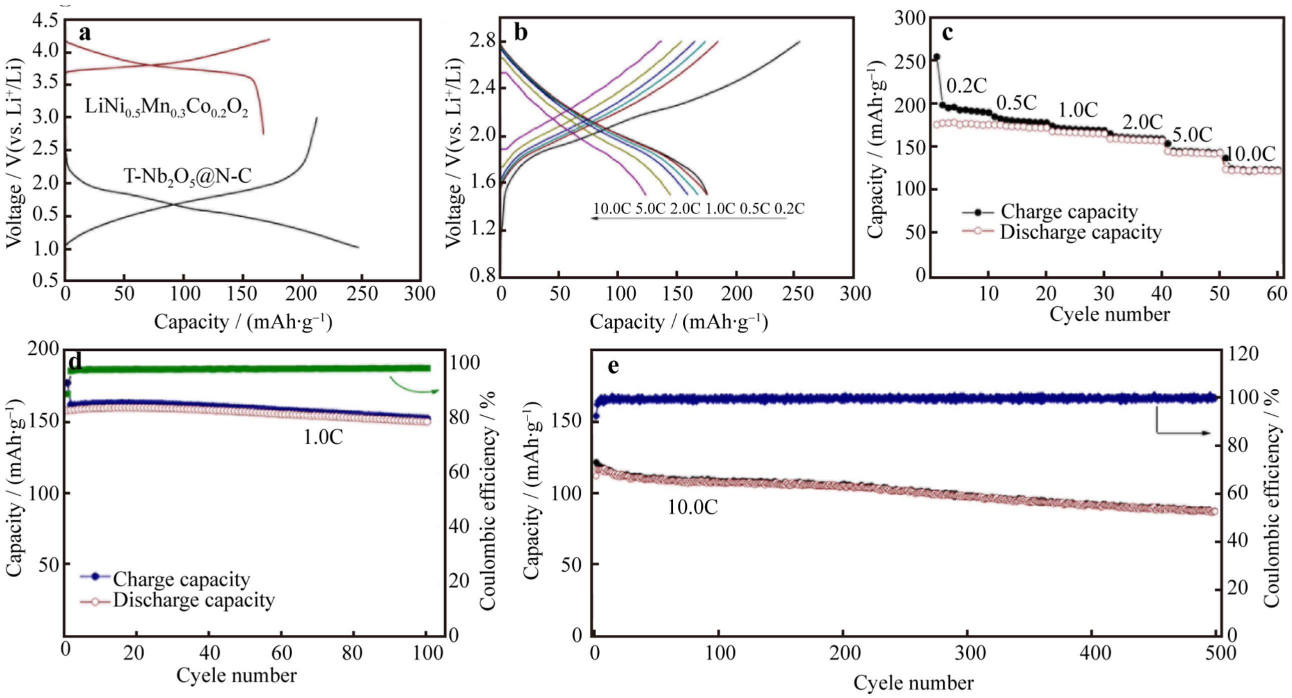

Fig. 6 **a** Charge–discharge curves of $LiNi_{0.5}Mn_{0.3}Co_{0.2}O_4$/Li and $T\text{-}Nb_2O_5$@N–C/Li half cells at 0.2C; **b** charge–discharge curves and **c** rate performance of $LiNi_{0.5}Mn_{0.3}Co_{0.2}O_4$||$T\text{-}Nb_2O_5$@N–C full cell at different current rates; cyclability of $LiNi_{0.5}Mn_{0.3}Co_{0.2}O_4$||$T\text{-}Nb_2O_5$@N–C full cell at **d** 1.0C over 100 cycles and **e** 10.0C over 500 cycles

(pseudocapacitive). Furthermore, Eq. (4) was adopted to quantitatively analyze the contributions of diffusion and capacitive behavior [40].

$$i = k_1 v + k_2 v^{1/2} \tag{4}$$

where $k_1 v$ and $k_2 v^{1/2}$ are represent the surface-controlled capacitive behavior and diffusion-dominated process, respectively. Therefore, the pseudocapacitive contribution ratio can be calculated by $k_1 v/i$. According to the analysis, pseudocapacitive contribution raises 56.4% of the capacity storage of $T\text{-}Nb_2O_5$@N–C at 0.2 $mV \cdot s^{-1}$, as demonstrated in Fig. 5e (green region). Moreover, the pseudocapacitive contribution gradually further enlarges from 56.4% to 91.1% with the scan rate increasing from 0.2 to 5.0 $mV \cdot s^{-1}$, as shown in Fig. 5f. In contrast, the capacitive contributions are extremely higher than those of $T\text{-}Nb_2O_5$ (Fig. S3). More importantly, $T\text{-}Nb_2O_5$@N–C exhibits pseudocapacitance dominant charge transfer behavior, resulting in the long-life cyclability and superior rate performance.

For the actual application of the as-prepared material, full cell is necessary to be investigated. $LiNi_{0.5}Mn_{0.3}Co_{0.2}O_4$ was designed as the cathode to match with $T\text{-}Nb_2O_5$@N–C anode. The $LiNi_{0.5}Mn_{0.3}Co_{0.2}O_4$/Li half cells show a reversible capacity of 172.5 $mAh \cdot g^{-1}$ at 0.2C within 2.75–4.20 V (Fig. 6a). The mass of cathode material is excessive, so the performance of $T\text{-}Nb_2O_5$@N–C material is the key to the capacity in the full cell. Figure 6b, c shows large reversible capacities of 175.7, 175.5, 167.9, 159.2, 144.5 and 123.6 $mAh \cdot g^{-1}$ at 0.2C, 0.5C, 1.0C, 2.0C, 5.0C and 10.0C in full cell, respectively. After 100 cycles, up to 95.0% of the initial capacity is retained (Fig. 6d). When cycled at such a high current density (5C), the full cell still achieves higher capacity retention of 77.7% over 500 cycles, as shown in Fig. 6e. The rate capacity of this work is more superior to those previous reports [41, 42]. Therefore, $T\text{-}Nb_2O_5$@N–C is expected to become a practical anode material for the LIBs of electric vehicles.

4 Conclusion

In summary, the porous ultrathin N-doped carbon-coated $T\text{-}Nb_2O_5$@N–C was fabricated by a sample and effective approach with ionic liquids as a carbon and nitrogen source. $T\text{-}Nb_2O_5$@N–C presents excellent rate performance with a discharge capacity of 155.5 $mAh \cdot g^{-1}$ at 20C. Meanwhile, it exhibits a long-term cycling life with a discharge capacity of 101.1 $mAh \cdot g^{-1}$ at 10.0C after 2000 cycles. It is confirmed that ultrathin N-doped carbon coating for $T\text{-}Nb_2O_5$ not only endows the fast electrons and ions transport channels and buffers the volume changes under the long-term cycling process, but also can further yield excellent Li^+ intercalation pseudocapacitive property with high rate capability. The $LiNi_{0.5}Mn_{0.3}Co_{0.2}O_4$||T-$Nb_2O_5$@N–C full cell also exhibits good electrochemical performance. Therefore, the proposed synthesis methodology gives a simple, effective and scalable way to construct carbon-based composites for practical application.

Acknowledgements This work was financially supported by the National Natural Science Foundation of China (No. 21501101), the Natural Science Foundation of Henan Province (No. 182300410226), the Technological Project of Henan Province (Nos. 172102210426, 172102210423 and 182102310068) and the Education Department Project of Henan Province (No. 16A150038).

References

[1] Simon P, Gogotsi Y, Dunn B. Where do batteries end and supercapacitors begin. Science. 2014;343(6176):1210.

[2] Gu L, Xiao D, Hu YS, Li H, Ikuhara Y. Atomic-scale structure evolution in a quasi-equilibrated electrochemical process of electrode materials for rechargeable batteries. Adv Mater. 2015; 27(13):2134.

[3] Zhao Y, Liu J, Horn M, Motta N, Hu M, Li Y. Recent advancements in metalorganic framework based electrodes for supercapacitors. Sci China Mater. 2018;61:159.

[4] Larcher D, Tarascon JM. Towards greener and more sustainable batteries for electrical energy storage. Nat Chem. 2015;7(1):19.

[5] Li B, Zheng J, Zhang H, Jin L, Yang D, Lv H, Shen C, Shellikeri A, Zheng Y, Gong R, Zheng JP, Zhang C. Electrode materials, electrolytes, and challenges in nonaqueous lithium-ion capacitors. Adv Mater. 2018;30(17):1705670.

[6] Goodenough JB. Electrochemical energy storage in a sustainable modern society. Energy Environ Sci. 2014;7(1):14.

[7] Sivakkumar SR, Nerkar JY, Pandolfo AG. Rate capability of graphite materials as negative electrodes in lithium-ion capacitors. Electrochim Acta. 2010;55(9):3330.

[8] Sun R, Liu G, Cao S, Dong B, Liu X, Hu M, Liu M, Duan X. High rate capability performance of ordered mesoporous $TiNb_6O_{17}$ microsphere anodes for lithium ion batteries. Dalton Trans. 2017;46(48):17061.

[9] Liu GY, Zhao YY, Tang YF, Liu XD, Liu M, Wu PJ. In situ sol-gel synthesis of $Ti_2Nb_{10}O_{29}$/C nanoparticles with enhanced pseudocapacitive contribution for a high-rate lithium-ion battery. Rare Met. 2020;39(9):1072.

[10] Liu G, Liu X, Wang L, Ma J, Xie H, Ji X, Guo J, Zhang R. Hierarchical $Li_4Ti_5O_{12}$-TiO_2 microspheres assembled from nanoflakes with exposed $Li_4Ti_5O_{12}$ (011) and anatase TiO_2 (001) facets for high-performance lithium-ion batteries. Electrochim Acta. 2016;222:1103.

[11] Yan L, Rui X, Chen G, Xu W, Zou G, Luo H. Recent advances in nanostructured Nb-based oxides for electrochemical energy storage. Nanoscale. 2016;8(16):8443.

[12] Li HH, Saini A, Xu RY, Wang N, Lv XX, Wang YP, Yang T, Chen L, Jiang HB. Hierarchical Fe_3O_4@C nanofoams derived from metal-organic frameworks for high-performance lithium storage. Rare Met. 2020;39(9):1063.

[13] Zheng F, Wei L. Synthesis of ultrafine Co_3O_4 nanoparticles encapsulated in nitrogen-doped porous carbon matrix as anodes for stable and long-life lithium ion battery. J Alloy Compd. 2019;790:955.

[14] Zhang W, Zhang B, Jin H, Li P, Zhang Y, Ma S, Zhang J. Waste eggshell as bio-template to synthesize high capacity δ-MnO_2 nanoplatelets anode for lithium ion battery. Ceram Int. 2018; 44(16):20441.

[15] Jia C, Zhang X, Yang P. Anatase/rutile-TiO_2 hollow hierarchical architecture modified by SnO_2 toward efficient lithium storage. Int J Hydrogen Energy. 2018;43(4):2237.

[16] Wang X, Li G, Chen Z, Augustyn V, Ma X, Wang G, Dunn B, Lu Y. High-performance supercapacitors based on nanocomposites of Nb_2O_5 nanocrystals and carbon nanotubes. Adv Energy Mater. 2011;1(6):1089.

[17] Kim K, Woo SG, Jo YN, Lee J, Kim JH. Niobium oxide nanoparticle core-amorphous carbon shell structure for fast reversible lithium storage. Electrochim Acta. 2017;240:316.

[18] Lou SF, Cheng XQ, Wang L, Gao JL, Li Q, Ma YL, Gao YZ, Zuo PJ, Du CY, Yin GP. High-rate capability of three-dimensionally ordered macroporous T-Nb_2O_5 through Li^+ intercalation pseudocapacitance. J Power Sources. 2017;361:80.

[19] Fu SD, Yu Q, Liu ZH, Hu P, Chen Q, Feng SH, Mai LQ, Zhou L. Yolk–shell Nb_2O_5 microspheres as intercalation pseudocapacitive anode materials for high-energy Li-ion capacitors. J Mater Chem A. 2019;7(18):11234.

[20] Wu N, Du W, Gao X, Zhao L, Liu G, Liu X, Wu H, He YB. Hollow SnO_2 nanospheres with oxygen vacancies entrapped by a N-doped graphene network as robust anode materials for lithium-ion batteries. Nanoscale. 2018;10(24):11460.

[21] Hou H, Banks CE, Jing M, Zhang Y, Ji X. Carbon quantum dots and their derivative 3D porous carbon frameworks for sodium-ion batteries with ultralong cycle life. Adv Mater. 2016; 27(47):7861.

[22] Hong WW, Ge P, Jiang YL, Tian YL, Y, Zou GQ, Cao XY, Hou HS, Ji XB. Yolk-shell structured bismuth@N-doped carbon anode for lithium-ion battery with high volumetric capacity. ACS Appl Mater Interfaces. 2019;11(11):10829.

[23] Zhao L, Hu YS, Li H, Wang ZX, Chen LQ. Porous $Li_4Ti_5O_{12}$ coated with N-doped carbon from ionic liquids for Li-ion batteries. Adv Mater. 2011;23(11):1385.

[24] Lee JS, Wang XQ, Luo HM, Baker GA, Dai S. Facile ionothermal synthesis of microporous and mesoporous carbons from task specific ionic liquids. J Am Chem Soc. 2019;131(13): 4596.

[25] Meng JS, He Q, Xu LH, Zhang XC, Liu F, Wang XP, Li Q, Xu XM, Zhang GB, Niu CJ, Xiao ZT, Liu ZA, Zhu ZZ, Zhao Y, Mai LQ. Identification of phase control of carbon-confined Nb_2O_5 nanoparticles toward high-performance lithium storage. Adv Energy Mater. 2019;9(18):1802695.

[26] Lübke M, Sumboja A, Johnson ID, Brett DJL, Shearing PR, Liu ZL, Darr JA. High power nano-Nb_2O_5 negative electrodes for lithium-ion batteries. Electrochim Acta. 2016;192:363.

[27] Lim E, Jo C, Kim H, Mun Y, Chun J, Ye Y, Hwang J, Ha K-S, Roh KC, Kang K, Yoon S, Lee J. Facile synthesis of Nb_2O_5@carbon core-shell nanocrystals with controlled crystalline structure for high-power anodes in hybrid supercapacitors. ACS Nano. 2015;9(7):7497.

[28] Bitencourt CS, Luz AP, Pagliosa C, Pandolfelli VC. Role of catalytic agents and processing parameters in the graphitization process of a carbon-based refractory binder. Ceram Int. 2015; 41(10):13320.

[29] Fang YJ, Xiao LF, Ai XP, Cao YL, Yang HX. Hierarchical carbon framework wrapped $Na_3V_2(PO_4)_3$ as a superior high-rate and extended lifespan cathode for sodium-ion batteries. Adv Mater. 2015;27(39):5895.

[30] Jiao XY, Hao QL, Xia XF, Wu ZD, Lei W. Metal organic framework derived Nb_2O_5@C nanoparticles grown on reduced graphene oxide for high-energy lithium ion capacitors. Chem Commun. 2019;55(18):2692.

[31] Augustyn V, Come J, Lowe MA, Kim JW, Taberna PL, Tolbert SH, Abruna HD, Simon P, Dunn B. High-rate electrochemical

energy storage through Li^+ intercalation pseudocapacitance. Nat Mater. 2013;12(6):518.

[32] Zhao W, Zhao W, Zhu G, Lin T, Xu F, Huang F. Black Nb_2O_5 nanorods with improved solar absorption and enhanced photocatalytic activity. Dalton Trans. 2016;45(9):3888.

[33] Hemmati S, Li G, Wang XL, Ding YL, Pei Y, Yu AP, Chen ZW. 3D N-doped hybrid architectures assembled from 0D T-Nb_2O_5 embedded in carbon microtubes toward high-rate Li-ion capacitors. Nano Energy. 2019;56:118.

[34] Li SY, Wang T, Zhu WQ, Lian JB, Huang YP, Yu YY, Qiu JX, Zhao Y, Yong YC, Lia HM. Controllable synthesis of uniform mesoporous H-Nb_2O_5/rGO nanocomposites for advanced lithium ion hybrid supercapacitors. J Mater Chem A. 2019;7(2): 693.

[35] Shi YH, Li XY, Zhang WD, Li HH, Wang SG, Wu XL, Su ZM, Zhang JP, Sun HZ. Micron-scaled MoS_2/N-C particles with embedded nano-MoS_2: a high-rate anode material for enhanced lithium storage. Appl Surf Sci. 2019;486:519.

[36] Biemolt J, Denekamp IM, Slot TK, Rothenberg G, Eisenberg D. Boosting the supercapacitance of nitrogen-doped carbon by tuning surface functionalities. Chemsuschem. 2017;10(20):4018.

[37] Zhao YJ, Ding CH, Hao YN, Zhai XM, Wang CZ, Li YT, Li JB, Jin HB. Neat design for the structure of electrode to optimize the lithium-ion battery performance. ACS Appl Mater Interfaces. 2018;10(32):27106.

[38] Cao DP, Zhang JC, Liu JJ, Zhang JC, Li CL. H-Nb_2O_5 wired by tetragonal tungsten bronze related domains as high-rate anode for Li-ion batteries. Energy Storage Mater. 2018;11:152.

[39] Deng BH, Lei TY, Zhu WH, Xiao L, Liu JP. In-plane assembled orthorhombic Nb_2O_5 nanorod films with high-rate Li^+ intercalation for high-performance flexible Li-ion capacitors. Adv Funct Mater. 2018;28(1):1704330.

[40] Brezesinski T, Wang J, Tolbert SH, Dunn B. Ordered mesoporous α-MoO_3 with iso-oriented nanocrystalline walls for thin-film pseudocapacitors. Nat Mater. 2010;9(2):146.

[41] Zhu XZ, Cao HJ, Li RJ, Fu QF, Liang GS, Chen YJ, Luo LJ, Lin CF, Zhao XS. Zinc niobate materials: crystal structures, energy-storage capabilities and working mechanisms. J Mater Chem A. 2019;7(44):25537.

[42] Fu QF, Li RJ, Zhu XZ, Liang GS, Luo LJ, Chen YJ, Lin CF, Zhao XS. Design, synthesis and lithium-ion storage capability of $Al_{0.5}Nb_{24.5}O_{62}$. J Mater Chem A. 2019;7(34):19862.